ADVANCED MATERIALS
www.advmat.de

In-Plane Anisotropic Thermal Conductivity of Few-Layered Transition Metal Dichalcogenide Td-WTe_2

Yu Chen, Bo Peng, Chunxiao Cong, Jingzhi Shang, Lishu Wu, Weihuang Yang, Jiadong Zhou, Peng Yu, Hongbo Zhang, Yanlong Wang, Chenji Zou, Jing Zhang, Sheng Liu, Qihua Xiong, Hezhu Shao, Zheng Liu,* Hao Zhang,* Wei Huang, and Ting Yu**

2D Td-WTe_2 has attracted increasing attention due to its promising applications in spintronic, field-effect chiral, and high-efficiency thermoelectric devices. It is known that thermal conductivity plays a crucial role in condensed matter devices, especially in 2D systems where phonons, electrons, and magnons are highly confined and coupled. This work reports the first experimental evidence of in-plane anisotropic thermal conductivities in suspended Td-WTe_2 samples of different thicknesses, and is also the first demonstration of such anisotropy in 2D transition metal dichalcogenides. The results reveal an obvious anisotropy in the thermal conductivities between the zigzag and armchair axes. The theoretical calculation implies that the in-plane anisotropy is attributed to the different mean free paths along the two orientations. As thickness decreases, the phonon-boundary scattering increases faster along the armchair direction, resulting in stronger anisotropy. The findings here are crucial for developing efficient thermal management schemes when engineering thermal-related applications of a 2D system.

Layered transition metal dichalcogenides (TMDs), whose transition metal atoms are sandwiched between two chalcogen layers, have drawn widespread attention in the field of condensed matter physics.[1] These van der Waals materials exhibit fascinating optical, electronic, and thermal properties when they are thinned down from bulk crystals to an atomically thin layer.[2–5] Naturally formed tungsten ditelluride (WTe_2) has been proven to have the lowest energy in the Td-polytype, a distorted 1T phase, and exhibits semimetallic properties.[6,7] Excitingly, nonmagnetic Td-WTe_2 has been brought to the attention of researchers due to recent experiments that discovered its extremely large and nonsaturating positive magnetoresistance at low temperatures, where the magnetoresistance increases up to 1.3×10^7% at 60 T without

Dr. Y. Chen, Prof. W. Huang
Shaanxi Institute of Flexible Electronics (SIFE)
Northwestern Polytechnical University (NPU)
Xi'an 710129, China

Dr. Y. Chen, Dr. J. Shang, L. Wu, H. Zhang, C. Zou, Dr. J. Zhang, S. Liu, Prof. Q. Xiong, Prof. T. Yu
Division of Physics and Applied Physics
School of Physical and Mathematical Sciences
Nanyang Technological University
Singapore 637371, Singapore
E-mail: yuting@ntu.edu.sg

B. Peng, Prof. H. Zhang
Key Laboratory of Micro and Nano Photonic Structures (MOE)
Department of Optical Science and Engineering
Fudan University
Shanghai 200433, China
E-mail: zhangh@fudan.edu.cn

Prof. C. Cong
State Key Laboratory of ASIC and System
School of Information Science and Technology
Fudan University
Shanghai 200433, China
E-mail: cxcong@fudan.edu.cn

The ORCID identification number(s) for the author(s) of this article can be found under https://doi.org/10.1002/adma.201804979.

DOI: 10.1002/adma.201804979

Prof. W. Yang
Key Laboratory of RF Circuits and System of Ministry of Education
Hangzhou Dianzi University
Hangzhou 310018, China

Dr. J. Zhou, Dr. P. Yu, Prof. Z. Liu
School of Materials Science and Engineering
Nanyang Technological University
Singapore 639798, Singapore
E-mail: z.liu@ntu.edu.sg

Dr. Y. Wang
Key Laboratory of Chemical Lasers
Dalian Institute of Chemical Physics
Chinese Academy of Sciences
Dalian 116023, China

Prof. H. Shao
Ningbo Institute of Materials Technology and Engineering
Chinese Academy of Sciences
Ningbo 315201, China

Prof. W. Huang
Key Laboratory of Flexible Electronics (KLOFE) & Institute of Advanced Materials (IAM)
Nanjing Tech University (NanjingTech)
Nanjing 211800, China

any sign of saturation.[8] In addition, Zhou and co-workers observed that Td-WTe_2 could be completely transformed into the monoclinic 1T′ phase under high pressure, and superconductivity was found in the 1T′ phase when the pressure was higher than 15.5 GPa.[9,10] Very recent studies have recognized that Td-WTe_2 is an ideal contact for 2D semiconductors to effectively tune the Schottky barrier due to its comparatively low work function.[11] All of these intriguing physical properties show the promising applications of Td-WTe_2 in nanoscale magnetic devices. It is known that the thermal transport properties are of great significance to the design and operation of these ultrathin nanodevices.[12] For instance, thermal conductivity plays a vital role in adjusting the heat dissipation and thermoelectric efficiency. One effective approach to improve the performance of thermoelectric and thermal insulating materials is to lower the thermal conductivity without impacting the electronic properties.[13] Specifically, ultralow thermal conductivity is crucial to avoiding hot reflux from the cold end of the material with respect to the heat source, which is crucial to achieving an enormous improvement in the energy conversion efficiency.[14] Semimetal Td-WTe_2 is theoretically predicted to have a low thermal conductivity because of its heavy atomic mass and low Debye temperature, which makes it a prominent candidate for thermoelectric materials.[15] Nonetheless, the studies on the in-plane thermal conductivity of Td-WTe_2 are still in the initial stages. The recent first-principles calculations predicted that anisotropy exists in the in-plane thermal conductivity of bulk Td-WTe_2 along different lattice directions, with a maximum value along the [010] direction (*a*-axis) whereas the minimum value is in the [100] direction (*b*-axis).[16] In contrast, Ma et al. revealed that the calculated anisotropic thermal conductivity of monolayer Td-WTe_2 has its maximum value along the *b*-axis.[17] The only experimental results to date indicated that the lateral thermal conductivity of Td-WTe_2 thin flakes is smaller than 2 W m^{-1} K^{-1} at room temperature without any anisotropy.[18,19] Although the distinct crystal structure of Td-WTe_2 implies notable anisotropic properties, experimental demonstrations of such in-plane anisotropic thermal conductivity are still lacking, even in layered 2D TMDs.[20] Moreover, the large discrepancy in both the theoretical calculations and experimental results also require further investigation.

To date, Raman spectroscopy has been the most conventional and nondestructive technique for characterization of the thermal conductivities of 2D materials.[21–23] The focused laser enables anharmonic lattice vibrations and thermal expansion due to the temperature increase.[24,25] The thermal conductivity can then be extracted by combining the temperature- and laser-induced phonon softening. In this work, suspended Td-WTe_2 layers with different thicknesses were systematically investigated using various types of optical probes. First, the crystal orientation (zigzag and armchair directions) is identified by linear polarization-dependent Raman spectroscopy and second harmonic generation (SHG). Then, in situ micro Raman spectroscopy is employed to reveal the thermal conductivities of the layers. To the best of our knowledge, the remarkable in-plane anisotropic thermal conductivities and layer dependency of

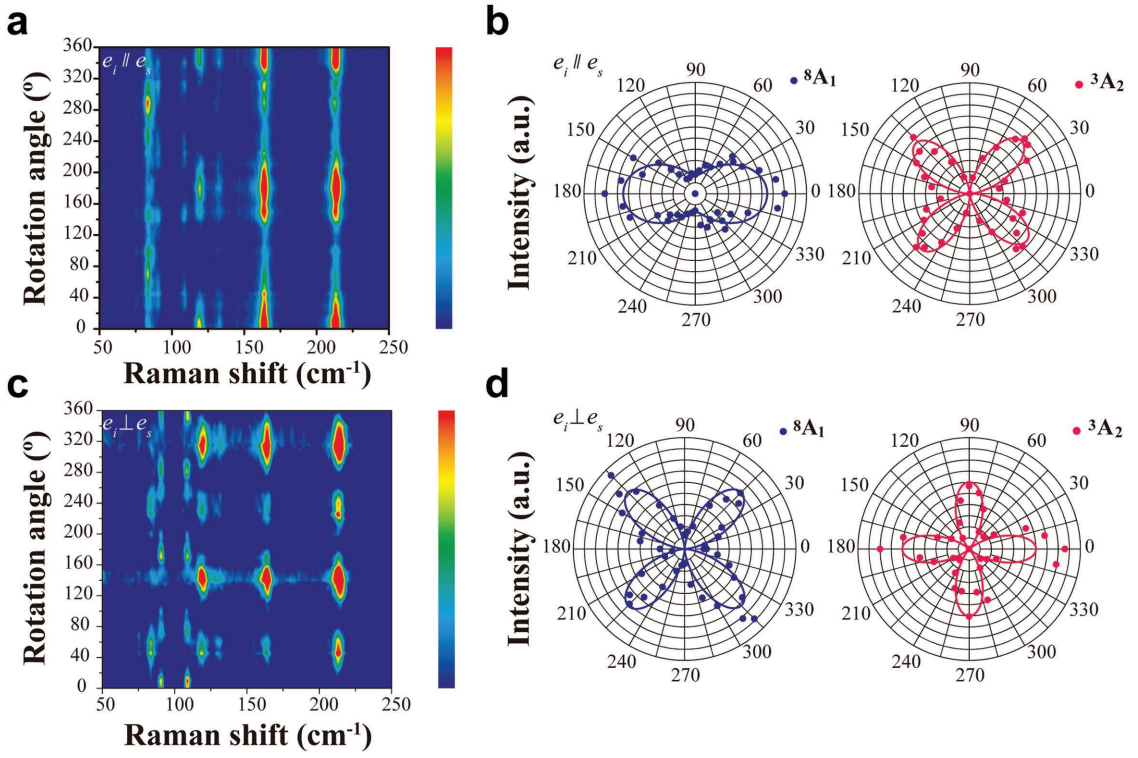

Figure 1. Angular-dependent Raman contour maps and polar plots of few-layered WTe_2. a,c) The contour maps of the angular-dependent Raman intensity of a Td-WTe_2 flake under the parallel-polarized configuration (a) and cross-polarized configuration (c). b,d) The polar plots and fit curves of the peak intensities in the two configurations. In $e_i \| e_s$, the intensity of the $^8A_1$ mode exhibits two-fold symmetry, while the intensity of the $^3A_2$ peak displays four-fold symmetry. In $e_i \perp e_s$, the angular dependences of both the $^8A_1$ and $^3A_2$ modes show four-fold symmetry patterns.

these 2D systems have been experimentally explored for the first time in this report. Theoretical modeling of the thermal conductivity in few-layered Td-WTe_2 reveals that the phonons along the armchair direction, which have a longer mean free path, are accountable for the suppression of the thermal conductivity. With decreasing thickness, the phonon-boundary scattering in the armchair orientation increased rapidly, further suppressing its thermal conductivity and leading to stronger anisotropy. Our findings remind us that we should carefully consider the anisotropic thermal effects when we develop 2D Td-WTe_2 nanoscale magnetic devices. The observation of the in-plane anisotropic thermal conductivities in the Td-WTe_2 layers is also the first demonstration of such interesting anisotropy in 2D TMDs, which should be meaningful for further exploring the potentials of 2D TMDs in thermoelectric devices.

The nonpolarized Raman spectra and irreducible representations of exfoliated Td-WTe_2 flakes on 300 nm SiO_2/Si substrate are shown in Figures S1 and S2 in the Supporting Information. The seven prominent Raman peaks are easily assigned by comparison with the theoretical predictions (Table S1, Supporting Information). The angular-dependent polarized Raman spectra and their peak intensities as a function of the rotation angle, θ, are shown in **Figure 1** and Figure S3 (Supporting Information). It is found that the intensities of nearly all of the Raman peaks demonstrate a periodical change as the sample was rotated. Figure 1a displays a contour map of the angular-dependent Raman intensity under the parallel-polarized configuration, where the incident light polarization (e_i) is parallel to the scattered light polarization (e_s). With the sample rotated from 0° to 360°, the intensities of the A_1 modes exhibit twofold symmetry, while the intensities of the A_2 modes display fourfold symmetry. For example, the polar plots and fit curves of the $^8A_1$ peak intensities clearly demonstrate that its intensity reaches maximum value at $\theta = 0°$ and 180°, as illustrated in Figure 1b, and the intensity of the $^3A_2$ mode has four maximums at 45°, 135°, 225°, and 315°. In the cross-polarized configuration ($e_i \perp e_s$), the angular dependences of both the A_1 and A_2 modes show fourfold symmetric patterns (Figure 1c,d; Figure S4, Supporting Information). Nevertheless, the polar plots and fit curves in Figure 1d reveal that the four-lobed shape of the $^8A_1$ mode is rotated by 45° with respect to that of the $^3A_2$ mode. Our experimental results are in strict accordance with the relationship between Raman tensors and laser polarizations, and imply the noteworthy anisotropic structure of Td-WTe_2, which could be used to conveniently and rapidly identify the zigzag and armchair directions of Td-WTe_2.[26]

Considering the obvious anisotropy of the lattice vibrational strength (phonon mode intensity) as revealed by the angular-dependent polarized Raman measurements, we hypothesize that the thermal conductivity of Td-WTe_2 may also exhibit anisotropy. To further investigate the anisotropic thermal conductivities of few-layered Td-WTe_2, it is of great significance to identify the crystalline orientation of the samples first. An exfoliated few-layered Td-WTe_2 flake was transferred onto a SiO_2/Si substrate with pre-etched holes, as shown in **Figure 2**a. The thickness and uniformity of the Td-WTe_2 flake were characterized by topological atomic force microscopy (AFM). The height profile shows that the thickness at the thinnest part is ≈11.2 nm (Figure S5, Supporting Information). Figure 2b depicts a schematic diagram of our experimental setup for the thermal conductivity measurements. To avoid unintentional damage to the suspended flake, before measuring the thermal conductivity of the suspended Td-WTe_2 flake, systematic measurements of the angular-dependent Raman spectroscopy and SHG under a parallel-polarized configuration were conducted on the supported side of the suspended sample by rotating the Td-WTe_2 flakes to identify its crystalline orientation (Figure S6, Supporting Information). The periodic polar response presented in both the Raman and SHG spectra clearly shows that the zigzag direction is along the sharp edge of the sample, which is initially aligned with the *x*-axis, as shown in Figure 2a (see details in the Supporting Information). Here, we identified the crystalline orientations of few-layered Td-WTe_2 by combining the angular-dependent Raman spectroscopy and SHG measurements, and this method could have great application prospects for other 2D materials, especially anisotropic crystal structures.

Considering the likely existence of in-plane anisotropic thermal conductivity in the ultrathin Td-WTe_2 layers, we performed in situ temperature dependent Raman spectroscopy under a linear polarization configuration, where the excitation laser polarization was aligned to the zigzag and armchair axes. Here, we only focus on the two pronounced Raman peaks at approximately 164 cm^{-1} ($^8A_1$) and 214 cm^{-1} ($^{10}A_1$). Figure 2c shows the Raman spectra along the zigzag-axis of an 11.2 nm-thick Td-WTe_2 flake with a temperature range from liquid nitrogen to room temperature. Both the $^8A_1$ and $^{10}A_1$ peaks have a drastic redshift with the increase in temperature, resulting from the anharmonic lattice vibrations and the thermal expansion.[27] The Lorentz fitting of these two Raman modes (Figure S7, Supporting Information) indicates that the $^{10}A_1$ mode at ≈214 cm^{-1} is more sensitive to the temperature change compared to the $^8A_1$ mode. This effect could be attributed to the high sensitivity of the $^{10}A_1$ mode to decreases in the interlayer coupling with increasing temperature.[27] Thus, the $^{10}A_1$ mode was chosen for further thermal conductivity studies. The evolution of the peak frequency, ω, as a function of the temperature was linearly fit by the equation $\omega = \omega_0 + \chi T$, where ω_0 is the Raman peak position at 0 K and the slope $\chi = \delta\omega/\delta T$ is the first-order temperature coefficient. The linearly fit results of the $^{10}A_1$ mode along both the zigzag and armchair directions are plotted in Figure 2d. The extracted first-order temperature coefficients are $\chi_{zigzag} = -0.01231$ and $\chi_{armchair} = -0.00889$ cm^{-1} K^{-1}, which are within the same order of magnitude as those reported in previous work.[27]

To reduce the heat dissipation of the substrate, the excitation laser power-dependent Raman spectra were studied for suspended Td-WTe_2. A prerequisite to extracting highly accurate thermal conductivities is for the hole under the sample to be adequately large. The size of the smallest hole in our measurements is 2.2 μm in diameter, which is sufficiently larger than the diameter of the laser spot (0.5 μm). The laser power-dependent Raman spectra of the suspended 11.2 nm thick sample are shown in Figure 2e. The excitation laser power was lower than 0.2 mW to avoid laser-induced damage. As the laser power increases, the rise in the local temperatures of the suspended films results in phonon softening. Figure 2f shows the frequency fitting of the $^{10}A_1$ mode at varying laser powers. The linear redshifts of the $^{10}A_1$ mode when probed along

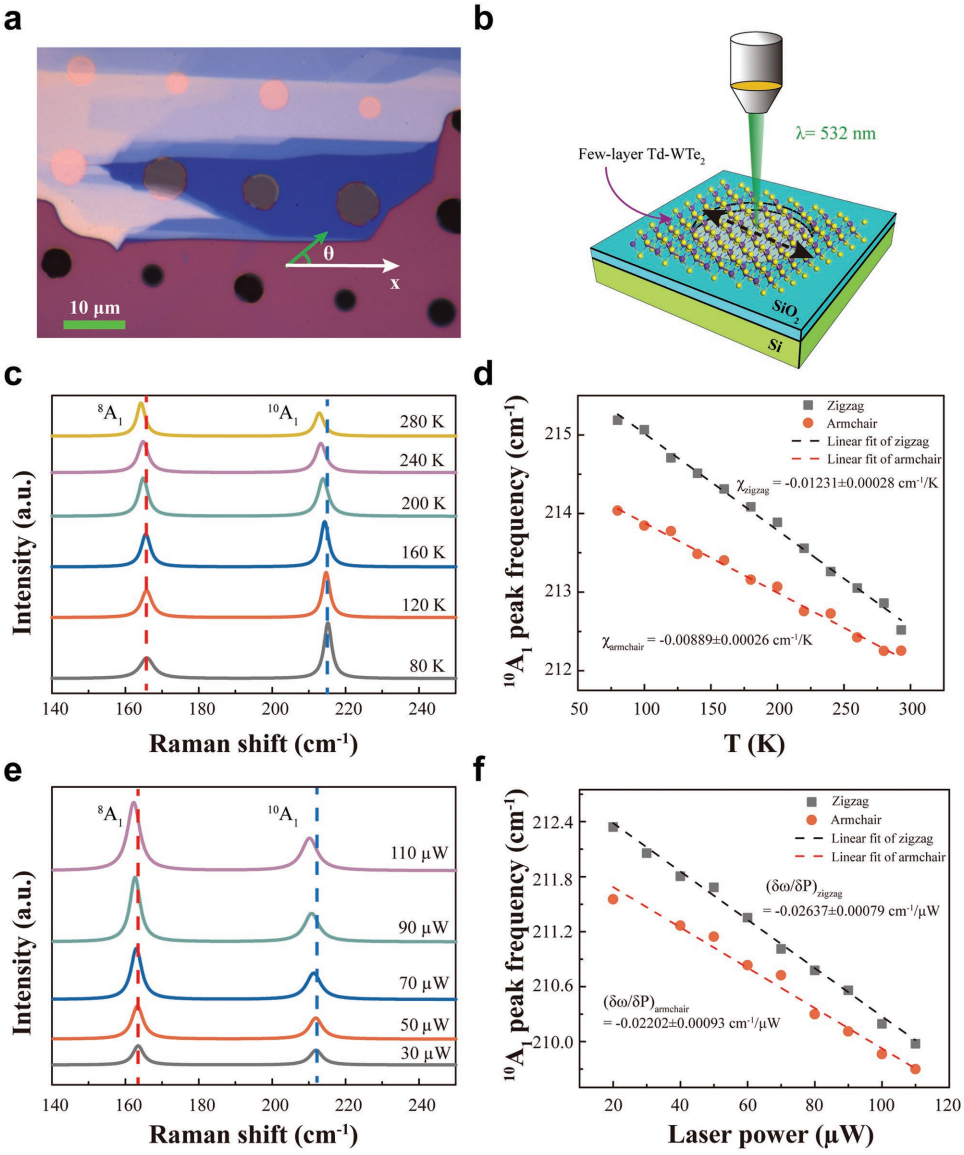

Figure 2. Temperature- and laser power-dependent Raman spectra of 11.2 nm thick suspended Td-WTe_2. a) Optical microscopy image of few-layered Td-WTe_2 flakes suspended on an array of holes. The angle between the laser polarization and the sample edge is defined as θ. b) Schematic diagram of the experimental setup for the thermal conductivity measurements. The black arrow represents the direction of the incident laser polarization. c) Temperature-dependent and e) excitation-laser-power-dependent Raman spectra of the 11.2 nm thick suspended Td-WTe_2 with incident laser polarization fixed along the zigzag direction. d,f) The linear fitting of the $^{10}A_1$ peak frequency as a function of temperature (d) and excitation laser power (f) along both the zigzag and armchair directions.

both crystalline orientations are clearly presented. The slopes $(\delta\omega/\delta P)$ are –0.02637 and –0.02202 cm^{-1} $(\mu W)^{-1}$ for the zigzag and armchair directions, respectively.

By solving the heat dissipation equations and considering the boundary conditions, the temperature diffusion at different laser powers can be obtained (more details are discussed in the Supporting Information). In our Raman experiments, the laser-induced weighted average temperature inside the laser spot is expressed as

$$T_m \approx \frac{\int_0^R T(r)q(r)r\,dr}{\int_0^R q(r)r\,dr} \quad (1)$$

where r is the distance between the position and the hole center, R is the radius of the hole, $T(r)$ is the temperature distribution inside the hole, and $q(r)$ indicates the volumetric optical heating.

Figure 3a shows the average temperature of a suspended 11.2 nm thick Td-WTe_2 flake as a function of the thermal conductivity under different excitation laser powers. Accordingly, the theoretical curve of $\delta T_m/\delta P$, which is related to the value of thermal conductivity, can be obtained, as shown in Figure 3b. The experimental value of $\delta T_m/\delta P$ is easily determined by the slope of both the temperature- and laser power-dependent redshifts of the $^{10}A_1$ mode. Thus, we can extract the thermal conductivity of suspended Td-WTe_2 by

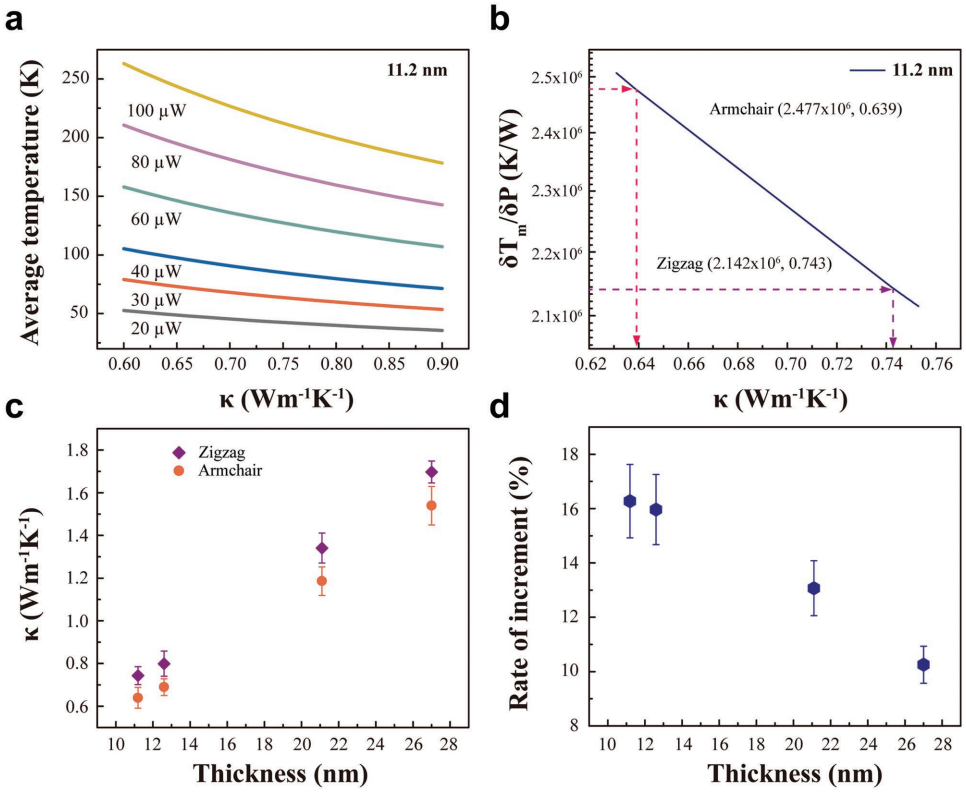

Figure 3. Anisotropic in-plane thermal conductivities of few-layered WTe_2. a) The weighted average temperature of suspended 11.2 nm thick Td-WTe_2 flakes versus the thermal conductivity under different laser powers. b) The calculated curve of $\delta T_m/\delta P$ as a function of the thermal conductivity. The thermal conductivities along the zigzag and armchair directions are extracted by plugging the experimentally obtained $\delta T_m/\delta P$ into the theoretical calculation. c) The extracted thermal conductivities along the zigzag and armchair directions of Td-WTe_2 with different thicknesses. d) The anisotropic difference in thermal conductivities as a function of the sample thickness. Error bars were evaluated from the standard deviation of the Raman peak position.

comparing the experimental value with the calculated curve of $\delta T_m/\delta P$. From the above measurements, the $\delta T_m/\delta P$ of 11.2 nm thick Td-WTe_2 along the zigzag and armchair directions are 2.142×10^6 and 2.477×10^6 K W^{-1}, respectively. As a result, the extracted thermal conductivity along the zigzag direction, κ_{zigzag} = 0.743 W m^{-1} K^{-1}, is 16.3% larger than that along the armchair direction, $\kappa_{armchair}$ = 0.639 W m^{-1} K^{-1}, showing a strong anisotropy in the thermal conductivity. The obtained thermal conductivities in our work are comparable with the previous results determined by the beam-offset-time-domain thermoreflectance (TDTR) technique.[18] Furthermore, we also extracted the thermal conductivities from other suspended samples of 12.6, 21.1, and 27.0 nm in thickness (Figure S8, Supporting Information), as summarized in Figure 3c. With increasing thickness, κ_{zigzag} rises to 1.697 W m^{-1} K^{-1} for the thickest film, an analogous tendency also appears in the armchair direction, where $\kappa_{armchair}$increases to a value of 1.539 W m^{-1} K^{-1}. Similar results have been verified in few-layered Bi_2Te_3 and black phosphorus.[28,29] Figure 3d shows that the in-plane anisotropy of the thermal conductivity becomes less remarkable as the thickness increases, which is reflected by a decreasing rate of the thermal conductivity increment $((\kappa_{zigzag} - \kappa_{armchair})/\kappa_{armchair})$ from 16.3% to 10.3%, resulting from the faster incremental increase of $\kappa_{armchair}$ with increasing thickness.

Theoretical calculations based on first principles and the Boltzmann transport equation (BTE) are performed to understand the thickness dependence of anisotropy in Td-WTe_2. For bulk Td-WTe_2, the calculated thermal conductivities along the *a*-, *b*-, and *c*-axis orientations are 14.93, 14.56, and 4.83 W m^{-1} K^{-1}, respectively. Previous experiments have shown that the in-plane thermal conductivity is 15 ± 3 W m^{-1} K^{-1} for Td-WTe_2 flakes with thicknesses greater than 500 nm,[18] verifying our calculations. Our calculated values are slightly higher than the previous ShengBTE results,[16] probably because of a larger supercell and cutoff in our calculations. In addition, in previous calculations, negative phonon frequencies are observed along the Γ–Y direction. Such negative frequencies may introduce large errors to the solution of the BTE. In our calculated phonon dispersion, there are no negative phonon frequencies, as shown in **Figure 4**a. We also calculated the lattice thermal conductivity of bulk Td-WTe_2 using relaxation time approximations (RTA). For all of the *a*-, *b*-, and *c*-axis orientations, RTA offers accurate conductivities within ≈5% of the full BTE counterparts. Because the RTA provides a reasonable estimation, we use this approach to calculate thin film thermal conductivities hereafter.

At 300 K, the number of thermally active phonon modes can be determined by the Bose–Einstein distribution function. The dotted white line shown in Figure 4a represents the frequency (145 cm^{-1}) below which the average phonon occupation number is greater than unity. To understand the role of these thermally active phonon modes, we calculate the in-plane cumulative thermal conductivity as a function of the phonon

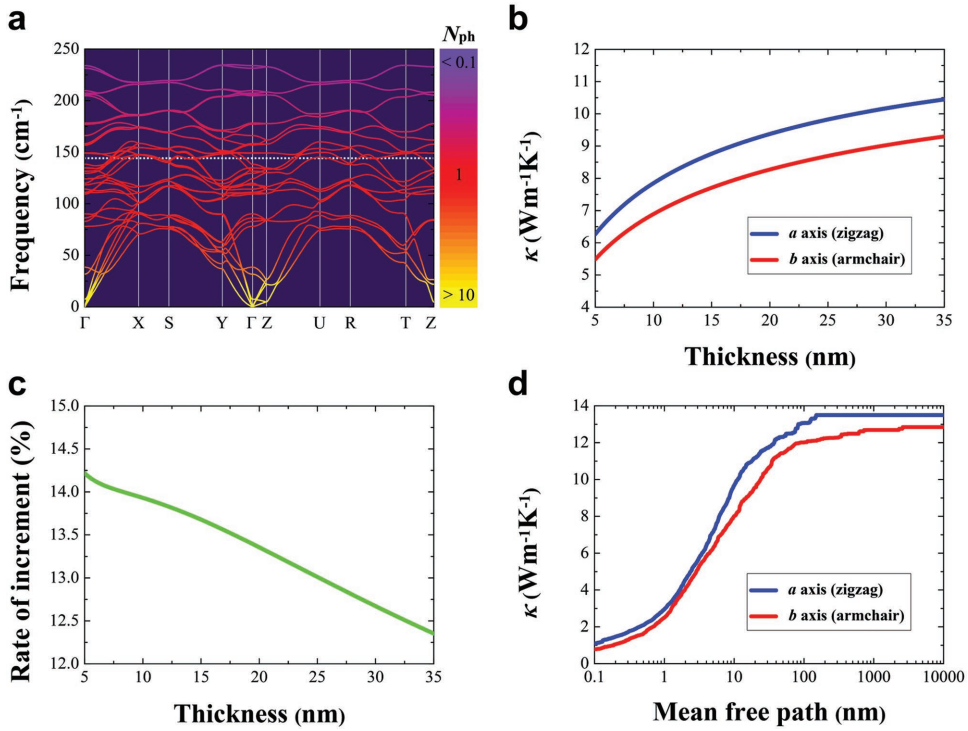

Figure 4. First principles modeling results for Td-WTe_2. a) Calculated phonon dispersion in bulk Td-WTe_2. The dotted white line represents the frequency below which the average phonon occupation number is greater than unity. The phonon occupation number is determined from the Bose–Einstein distribution function $n = 1/(e^{\hbar\omega/k_B T} - 1)$ at $T = 300$ K, where h is the Planck constant, ω is the phonon frequency, and k_B is the Boltzmann constant. b) Thin film thermal conductivity of Td-WTe_2. c) Calculated anisotropic ratio of κ as a function of film thickness. d) Cumulative κ as a function of the maximum mean free path along the *c*-axis orientation.

frequency. For both the *a*- and *b*-axis orientations, phonons below 145 cm^{-1} contribute to more than 95% of the total thermal conductivity.

Figure 4b presents the thin film lattice thermal conductivity of Td-WTe_2 computed for a $14 \times 14 \times 14$ wavevector grid. The κ value decreases for the thinner films. We further calculate the anisotropic ratio in κ along the *a*- and *b*-axis orientations (corresponding to the zigzag and armchair directions, respectively). As shown in Figure 4c, the anisotropy increases to 14% as the layer thickness becomes thinner than 7 nm. For comparison, the calculated anisotropic ratio is only 2.6% in bulk Td-WTe_2, which is consistent with the experimental observation that the in-plane thermal conductivity of Td-WTe_2 is isotropic at the bulk level.[18] This isotropy can be attributed to comparable group velocities along the *a*- and *b* -axis orientations (Figure S9, Supporting Information). Further questions arise as to why the anisotropy in Td-WTe_2 can only be observed in thinner films. It is worth investigating the microscopic origin of the thickness dependence of the transport anisotropy.

The effective in-plane thermal conductivity in a Td-WTe_2 film using the RTA approach can be evaluated as[30]

$$\kappa_{\text{eff}}(L) = \sum_{\text{k}} S_{\text{k}}(L) C_{\text{k}} \,||\, \boldsymbol{v}_{\text{k}} \,||\, \Lambda_{\text{k}} \cos^2\theta \tag{2}$$

where L is the film thickness, $S_k(L)$ is the wavevector-resolved suppression factor that accounts for phonon-boundary scattering, C_k is the mode contribution to heat capacity, $\boldsymbol{v}_k$ is the group velocity, Λ_k is the mean free path, and θ is the angle between the transport axis and $\boldsymbol{v}_k$. Using the effective Knudsen number[31]

$$K = \frac{\boldsymbol{v}_z / ||\, \boldsymbol{v} \,|| \cdot \boldsymbol{\Lambda}}{L} = \frac{\boldsymbol{\Lambda}_z}{L} \tag{3}$$

the suppression function becomes

$$S(L) = \frac{1 - p\mathrm{e}^{-1/K} - (1-p)K\left(1 - \mathrm{e}^{-1/K}\right)}{1 - p\mathrm{e}^{-1/K}} \tag{4}$$

where p varies with the surface conditions. Here, we assume the boundary acts as a diffuse scatterer that reradiates phonons in a random direction ($p = 0$), which has been done in the κ calculations of thin black phosphorus flakes due to the presence of surface disorder.[32] When $p = 0$, $S(L)$ becomes

$$S(L) = 1 - K\left(1 - \mathrm{e}^{-1/K}\right) \tag{5}$$

Obviously, $S(L)$ increases as K decreases, i.e., a thicker L and smaller $\boldsymbol{\Lambda}_z$ (lower $\boldsymbol{v}_z$ and smaller Λ). When L becomes thicker, K approaches zero, and $S(L)$ approaches one, corresponding to bulk transport. For phonons with $\boldsymbol{v}_z = 0$, K approaches zero as well, indicating that phonons that never interact with the film boundaries can transport all of their heat regardless of the film thickness. However, neither L nor $\boldsymbol{v}_z$ can directly influence the anisotropy of the phonon transport properties. Thus, we focus

on the mean free path, Λ_z, along the *a*- and *b*-axis directions hereafter.

We investigate the role of the mean free path, Λ_z, by calculating the cumulative thermal conductivity along the *c*-axis orientation

$$\kappa_{\alpha\alpha}(\Lambda_z^{\max}) = \frac{1}{\Omega}\sum_{k}^{\Lambda_z<\Lambda_z^{\max}} C_k v_{k\alpha}\Lambda_\alpha \quad (6)$$

where Ω is the volume of the unit cell, and α is the transport axis. The cumulative thermal conductivity of Td-WTe_2 is plotted in Figure 4d.

The mean free path, Λ_z, for *b*-axis transport is much longer than that for *a*-axis transport. This means that κ along the *b*-axis direction is more sensitive to the film thickness than that along the *a*-axis direction. Intuitively, phonons with shorter mean free paths cannot contribute to phonon-boundary scattering because they cannot reach the surfaces. A large Λ_z for the *b*-axis transport leads to strong phonon-boundary scattering and hence a reduced *S*, which further suppresses the thermal conductivity. Due to these longer mean free paths along the *b*-axis orientation, its *S* decreases faster than that along the *a*-axis orientation as the film thickness decreases, leading to stronger anisotropy. Consequently, the anisotropy of the thermal conductivity increases with decreasing thickness. It should be noted that in few-layered black phosphorus, the maximum mean free paths along the armchair and zigzag directions are comparable to each other.[29] Therefore, the thickness dependence of anisotropy in Td-WTe_2 shows a different trend when compared to that of black phosphorus.

To examine the universality of our findings, we consider an extreme case where the mean free path is in the small-grain limit. As the grain size further decreases, nanostructure-induced phonon scattering becomes dominant over three-phonon scattering, and the mean free path is uniformly limited to a constant value, ξ_{sg}. Therefore, the thermal conductivity, κ^{nano}, becomes proportional to ξ_{sg}[33]

$$\kappa^{nano} = \kappa_{sg}\xi_{sg} \quad (7)$$

where κ_{sg} is the small-grain-limit reduced thermal conductivity. The calculated κ_{sg} along the *a*- and *b*-axes is 0.59 and 0.37 W m^{-1} K^{-1} per unit length of the mean free path in the small-grain limit (nm), respectively. This indicates that at extremely small sizes, the in-plane anisotropy will further increase to 60.2%. The small-grain limit calculations verify the experimental results that the anisotropy increases as the layers become thinner.

In summary, we explored the anisotropic in-plane thermal conductivities of suspended few-layered Td-WTe_2 flakes by Raman spectroscopy for the first time. This is also the first experimental demonstration of such anisotropy in 2D TMDs. Considering the strong angular dependence of an anisotropic system, we first employed linear polarization-dependent Raman spectroscopy and SHG to identify the crystalline orientations (zigzag and armchair axes) of the Td-WTe_2 flakes. Next, we investigated the thermal conductivities of the Td-WTe_2 layers by in situ micro Raman spectroscopy and found thermal conductivities of 0.743 and 0.639 W m^{-1} K^{-1} in the 11.2 nm thick layer along the zigzag and the armchair axes, respectively. Phonons with different mean free paths along the zigzag and armchair directions are responsible for the in-plane anisotropic thermal conductivities. The studies of the thickness-dependent thermal conductivity further reveal that increases in the thickness could weaken such anisotropy as the thermal conductivities along both directions increase, which results from a longer mean free path along the armchair axis and hence less phonon-boundary scattering. The results shed more light on the applications of Td-WTe_2 and the design of efficient thermal management schemes in next-generation thermoelectric devices.

Supporting Information

Supporting Information is available from the Wiley Online Library or from the author.

Acknowledgements

Y.C. and B.P. contributed equally to this work. This work was mainly supported by Singapore MOE Tier 1 RG199/17. C.C. thanks the support of the National Young 1000 Talent Plan of China, the National Natural Science Foundation of China (No. 61774040), and the Shanghai Municipal Natural Science Foundation (No. 16ZR1402500). J.Z., P.Y., and Z.L. acknowledge the support MOE Tier 1 grant RG164/15, MOE Tier 2 grant MOE2016-T2-2-153 and MOE2015-T2-2-007, and Singapore National Research Foundation under NRF award number NRF-NRFF2013-08. W.H. thanks the support of the Natural Science Foundation of Jiangsu Province (BM2012010), Priority Academic Program Development of Jiangsu Higher Education Institutions (YX03001), Ministry of Education of China (IRT1148), Synergetic Innovation Center for Organic Electronics and Information Displays (61136003), the National Natural Science Foundation of China (51173081) and Fundamental Studies of Perovskite Solar Cells (2015CB932200).

Conflict of Interest

The authors declare no conflict of interest.

Keywords

2D transition-metal dichalcogenides, in-plane anisotropy, mean free paths, suspended Td-WTe_2, thermal conductivity

Received: August 1, 2018
Revised: December 9, 2018
Published online: December 27, 2018

[1] Q. H. Wang, K. Kalantar-Zadeh, A. Kis, J. N. Coleman, M. S. Strano, *Nat. Nanotechnol.* **2012**, *7*, 699.
[2] S. Manzeli, D. Ovchinnikov, D. Pasquier, O. V. Yazyev, A. Kis, *Nat. Rev. Mater.* **2017**, *2*, 17033.
[3] K. F. Mak, C. Lee, J. Hone, J. Shan, T. F. Heinz, *Phys. Rev. Lett.* **2010**, *105*, 136805.
[4] W. Fu, Y. Chen, J. Lin, X. Wang, Q. Zeng, J. Zhou, L. Zheng, H. Wang, Y. He, H. He, Q. Fu, K. Suenaga, T. Yu, Z. Liu, *Chem. Mater.* **2016**, *28*, 7613.

[5] H. Wang, Y. Chen, M. Duchamp, Q. Zeng, X. Wang, S. H. Tsang, H. Li, L. Jing, T. Yu, E. H. T. Teo, Z. Liu, *Adv. Mater.* **2018**, *30*, 1704382.
[6] C. H. Lee, E. C. Silva, L. Calderin, M. A. T. Nguyen, M. J. Hollander, B. Bersch, T. E. Mallouk, J. A. Robinson, *Sci. Rep.* **2015**, *5*, 10013.
[7] J. Augustin, V. Eyert, T. Böker, W. Frentrup, H. Dwelk, C. Janowitz, R. Manzke, *Phys. Rev. B* **2000**, *62*, 10812.
[8] M. N. Ali, J. Xiong, S. Flynn, J. Tao, Q. D. Gibson, L. M. Schoop, T. Liang, N. Haldolaarachchige, M. Hirschberger, N. Ong, *Nature* **2014**, *514*, 205.
[9] X. C. Pan, X. Chen, H. Liu, Y. Feng, Z. Wei, Y. Zhou, Z. Chi, L. Pi, F. Yen, F. Song, *Nat. Commun.* **2015**, *6*, 7805.
[10] Y. Zhou, X. Chen, N. Li, R. Zhang, X. Wang, C. An, Y. Zhou, X. Pan, F. Song, B. Wang, *AIP Adv.* **2016**, *6*, 075008.
[11] Y. Liu, P. Stradins, S. H. Wei, *Sci. Adv.* **2016**, *2*, e1600069.
[12] A. Taube, J. Judek, A. Łapińska, M. Zdrojek, *ACS Appl. Mater. Interfaces* **2015**, *7*, 5061.
[13] A. Majumdar, *Science* **2004**, *303*, 777.
[14] Y. Ma, M. Liu, A. Jaber, R. Y. Wang, *J. Mater. Chem. A* **2015**, *3*, 13483.
[15] G. A. Slack, *Solid State Phys.* **1979**, *34*, 1.
[16] G. Liu, H. Y. Sun, J. Zhou, Q. F. Li, X.-G. Wan, *New J. Phys.* **2016**, *18*, 033017.
[17] J. Ma, Y. Chen, Z. Han, W. Li, *2D Mater.* **2016**, *3*, 045010.
[18] Y. Zhou, H. Jang, J. M. Woods, Y. Xie, P. Kumaravadivel, G. A. Pan, J. Liu, Y. Liu, D. G. Cahill, J. J. Cha, *Adv. Funct. Mater.* **2017**, *27*, 1605928.
[19] M. J. Mleczko, R. L. Xu, K. Okabe, H.-H. Kuo, I. R. Fisher, H.-S. P. Wong, Y. Nishi, E. Pop, *ACS Nano* **2016**, *10*, 7507.
[20] X. Ma, P. Guo, C. Yi, Q. Yu, A. Zhang, J. Ji, Y. Tian, F. Jin, Y. Wang, K. Liu, *Phys. Rev. B* **2016**, *94*, 214105.
[21] A. A. Balandin, S. Ghosh, W. Bao, I. Calizo, D. Teweldebrhan, F. Miao, C. N. Lau, *Nano Lett.* **2008**, *8*, 902.
[22] R. Yan, J. R. Simpson, S. Bertolazzi, J. Brivio, M. Watson, X. Wu, A. Kis, T. Luo, A. R. Hight Walker, H. G. Xing, *ACS Nano* **2014**, *8*, 986.
[23] N. Peimyoo, J. Shang, W. Yang, Y. Wang, C. Cong, T. Yu, *Nano Res.* **2015**, *8*, 1210.
[24] N. Bonini, M. Lazzeri, N. Marzari, F. Mauri, *Phys. Rev. Lett.* **2007**, *99*, 176802.
[25] I. Calizo, A. Balandin, W. Bao, F. Miao, C. Lau, *Nano Lett.* **2007**, *7*, 2645.
[26] X.-L. Liu, X. Zhang, M.-L. Lin, P.-H. Tan, *Chin. Phys. B* **2017**, *26*, 422.
[27] M. K. Jana, A. Singh, D. J. Late, C. R. Rajamathi, K. Biswas, C. Felser, U. V. Waghmare, C. Rao, *J. Phys.: Condens. Matter* **2015**, *27*, 285401.
[28] M. T. Pettes, J. Maassen, I. Jo, M. S. Lundstrom, L. Shi, *Nano Lett.* **2013**, *13*, 5316.
[29] Z. Luo, J. Maassen, Y. Deng, Y. Du, R. P. Garrelts, M. S. Lundstrom, D. Y. Peide, X. Xu, *Nat. Commun.* **2015**, *6*, 8572.
[30] J. Carrete, B. Vermeersch, A. Katre, A. van Roekeghem, T. Wang, G. K. Madsen, N. Mingo, *Comput. Phys. Commun.* **2017**, *220*, 351.
[31] E. Ziambaras, P. Hyldgaard, *J. Appl. Phys.* **2006**, *99*, 054303.
[32] B. Smith, B. Vermeersch, J. Carrete, E. Ou, J. Kim, N. Mingo, D. Akinwande, L. Shi, *Adv. Mater.* **2017**, *29*, 1603756.
[33] W. Li, J. Carrete, N. A. Katcho, N. Mingo, *Comput. Phys. Commun.* **2014**, *185*, 1747.